IEEE Access
Multidisciplinary | Rapid Review | Open Access Journal

SPECIAL SECTION ON EMERGING TECHNOLOGIES ON VEHICLE TO EVERYTHING (V2X)

Received November 15, 2018, accepted December 22, 2018, date of publication January 15, 2019, date of current version February 8, 2019.

Digital Object Identifier 10.1109/ACCESS.2019.2893136

Position-Specific Statistics of 60 GHz Vehicular Channels During Overtaking

ERICH ZÖCHMANN[1,2,3], (Member, IEEE), MARKUS HOFER[4], (Student Member, IEEE), MARTIN LERCH[2], (Student Member, IEEE), STEFAN PRATSCHNER[1,2], (Student Member, IEEE), LAURA BERNADÓ[4], (Member, IEEE), JIRI BLUMENSTEIN[3], (Member, IEEE), SEBASTIAN CABAN[2], SEUN SANGODOYIN[5], (Student Member, IEEE), HERBERT GROLL[2], (Student Member, IEEE), THOMAS ZEMEN[4], (Senior Member, IEEE), ALEŠ PROKEŠ[3], MARKUS RUPP[2], (Fellow, IEEE), ANDREAS F. MOLISCH[5], (Fellow, IEEE), AND CHRISTOPH F. MECKLENBRÄUKER[2], (Senior Member, IEEE)

[1]Christian Doppler Laboratory for Dependable Wireless Connectivity for the Society in Motion, Institute of Telecommunications, TU Wien, 1040 Vienna, Austria
[2]Institute of Telecommunications, TU Wien, 1040 Vienna, Austria
[3]Department of Radio Electronics, TU Brno, 616 00 Brno, Czech Republic
[4]Center for Digital Safety & Security, AIT Austrian Institute of Technology, 1210 Vienna, Austria
[5]Ming Hsieh Department of Electrical Engineering, University of Southern California, Los Angeles, CA 90007, USA

Corresponding author: Erich Zöchmann (ezoechma@nt.tuwien.ac.at)

This work was supported in part by the Austrian Federal Ministry for Digital and Economic Affairs, in part by the National Foundation for Research, Technology and Development, in part by the Czech Science Foundation under Project 17-27068S and Project 17-18675S, and in part by the National Sustainability Program under Grant LO1401. The work of S. Sangodoyin and A. F. Molisch was supported in part by NSF under Grant CNS-1457340, and in part by NIST under Grant 70NANB17H157. The authors acknowledge the TU Wien University Library for financial support through its Open Access Funding Program. For this research, the infrastructure of the SIX Center was used. This work was carried out in the framework of COST Action CA15104 IRACON.

ABSTRACT The time-variant vehicle-to-vehicle radio propagation channel in the frequency band from 59.75 to 60.25 GHz has been measured in an urban street in the city center of Vienna, Austria. We have measured a set of 30 vehicle-to-vehicle channel realizations to capture the effect of an overtaking vehicle. Our experiment was designed for characterizing the large-scale fading and the small-scale fading depending on the overtaking vehicle's position. We demonstrate that large overtaking vehicles boost the mean receive power by up to 10 dB. The analysis of the small-scale fading reveals that the two-wave with diffuse power (TWDP) fading model is adequate. By means of the model selection, we demonstrate the regions where the TWDP model is more favorable than the customarily used the Rician fading model. Furthermore, we analyze the time selectivity of our vehicular channel. To precisely define the Doppler and delay resolutions, a multitaper spectral estimator with discrete prolate spheroidal windows is used. The delay and Doppler profiles are inferred from the estimated local scattering function. Spatial filtering by the transmitting horn antenna decreases the delay and Doppler spread values. We observe that the RMS Doppler spread is below one-tenth of the maximum Doppler shift 2f v/c. For example, at 60 GHz, a relative speed of 30 km/h yields a maximum Doppler shift of approximately 3300 Hz. The maximum RMS Doppler spread of all observed vehicles is 450 Hz; the largest observed RMS delay spread is 4 ns.

INDEX TERMS 5G mobile communication, automotive engineering, communication channels, fading channels, intelligent vehicles, millimeter wave propagation, millimeter wave measurement, multipath channels, RMS delay spread, RMS Doppler spread, parameter extraction, time-varying channels, two-wave with diffuse power fading, wireless communication.

I. INTRODUCTION

The idea of automated cars represents a tremendous attraction to both, industry and the research community. More than ten years ago, a first forward collision warning system based on a millimeter wave (mmWave) automotive radar was commercialized [3]. Nowadays, reliable mmWave communication systems, supporting vehicle-to-vehicle information exchange, are anticipated to be among the key enablers for automated vehicles [4]. Due to the large available bandwidth at mmWave bands, even raw sensor data exchange between vehicles is possible [4]. Millimeter wave vehicular communications has two main distinctive features as

compared to sub-6-GHz vehicular communications. Firstly, the use of directive antennas – at least at one link end – and secondly, the much higher maximum Doppler shift. This high maximum Doppler shift, being directly proportional to the carrier frequency, is also viewed as a possible stumbling stone for vehicular mmWave communications. It is, however, shown theoretically in [5] and [6] that directional antennas, anticipated for mmWaves, act as spatial filters. The Doppler spread, and hence the time-selectivity, may be drastically decreased by beamforming. Experimentally, this has first been demonstrated in our prior work [2].

A. LITERATURE REVIEW

The analysis of static mmWave channels is already well advanced, see for example [7]–[29]. For static environments, frequency-domain channel sounding methods based on vector network analyzers are frequently used [30]. However, channel sounding concepts with sufficient sampling rates of the time-varying channel have been so far only treated by a few research papers [1], [2], [31]–[34].

Interestingly, mmWave frequency bands have been candidates for vehicular communications already for several decades [35], [36]. Millimeter wave train-to-infrastructure path loss is measured in [35], mmWave vehicle-to-vehicle communication performance is studied in [36]. Both works use narrowband transmissions. In [37] and [38], the focus is on inter-vehicle path loss results. Recent advances on mmWave circuit technology [39] renewed the interest in vehicular mmWave communications [40] and for joint vehicular communication and radar [41]. In [42], vehicle-to-vehicle (V2V) channel measurements at 38 GHz and 60 GHz, using a channel sounder with 1 GHz bandwidth, have been conducted. The antennas in [42] were put into the bumpers, thereby the dominating multipath components (MPCs) are the line-of-sight (LOS) component, a road reflection, and a delayed component reflected at the guard rails. In [43], 73 GHz V2V large-scale fading and small-scale fading analysis is provided for approaching vehicles. Intra-vehicular Doppler spectra of vibrations appearing while the vehicle is in operation are shown in [44] and [45]. In [46], signal-to-noise ratio (SNR) fluctuations for 60 GHz transmissions with 5 MHz bandwidth in a vehicle-to-infrastructure scenario are investigated. Time-varying receive power and time-varying small-scale fading for vehicular channels at 5.6 GHz are addressed in [47].

B. CONTRIBUTIONS OF THIS PAPER

With this article, we contribute to the dynamic mmWave vehicle-to-vehicle channel research by analyzing the effect of an overtaking vehicle on the mmWave V2V wideband (510 MHz) channel. Our experiment in a real-world street environment is designed to make the experiment as controllable as possible. The wireless link is always LOS and unblocked. We demonstrate that the size and the relative position of the overtaking vehicle greatly influences the large-scale and small-scale fading parameters. Furthermore, Doppler dispersion is strongly suppressed by the transmit horn antenna. The data we analyze consist of channel impulse responses (CIRs) during the overtaking situations with 30 vehicles. For the statistical analysis we differentiate between cars, sport utility vehicles (SUVs), and trucks.

C. ORGANIZATION OF THIS PAPER

In Section II, we present our measurement scenario in detail. In Section III, we analyze the receive power fluctuations as a function of the relative position of the overtaking vehicle. Regardless of the position of the overtaking vehicle and its size, approximately 50% of the receive power belongs to the channel tap corresponding to the LOS delay. Accordingly, in the following Section IV, we analyze the small-scale fading of the LOS tap. The two-wave with diffuse power (TWDP) model is briefly introduced and we show that it explains our data very well. In Section V, we focus on delay and Doppler dispersion. The analysis of the root mean square (RMS) Doppler spread is based on the local scattering function (LSF). The obtained RMS Doppler spread values are then compared against RMS Doppler spread values of commonly used models. We conclude with simple channel modeling guidelines.

D. NOTATION

We mention here only notation that is not commonly in use. Estimated quantities are marked with $\hat{(\cdot)}$. Functions with discrete input variables are denoted by square brackets $f[\cdot]$; functions with continuous inputs are denoted by parentheses $f(\cdot)$. The floor function is indicated via $\lfloor\cdot\rfloor$ and the ceiling function is indicated via $\lceil\cdot\rceil$. "Corresponds to" is symbolized with $\triangleq$.

II. SCENARIO DESCRIPTION

We have measured a set of 60 GHz vehicle-to-vehicle channel realizations to capture the effect of an overtaking vehicle. The motivation for our setup is the scenario of two cars driving, one behind the other, keeping constant distance, and communicating via a 60 GHz mmWave link. A third vehicle then overtakes this car platoon and thus influences the wireless channel, depending on the overtaking car's relative position.[1] The vehicular channel data evaluated for this contribution consists of 30 different measurement runs. We are observing the effect of overtaking vehicles with excess speeds of up to 13 m/s. At the transmitter (TX) site, a horn antenna with an 18° half power beam width is used and aligned towards the receiver (RX) car. Surrounding buildings are filtered out by the directive horn antenna. At the RX site, a custom-built omni-directional ($\lambda/4$) monopole antenna is used. The RX has an omni-directional pattern so that scattered[2] waves from the passing vehicle are not filtered out. This situation occurs,

[1] Similar results will be obtained, if the car platoon overtakes a vehicle.

[2] By scattering we refer to any kind of wave interaction such as diffuse reflection or diffraction.

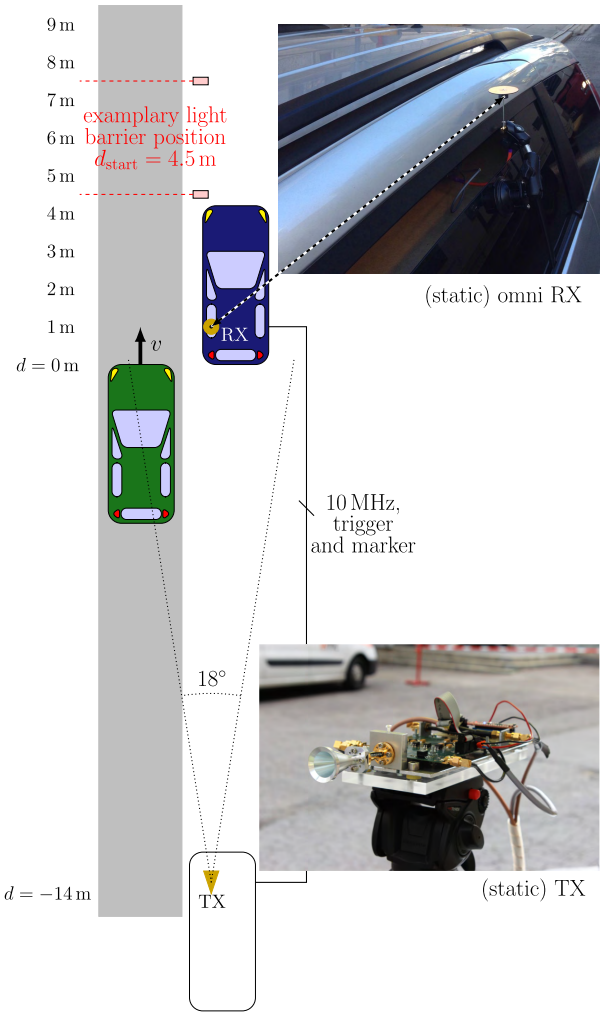

FIGURE 1. Bird's-eye view of the measurement site. TX and RX are static. The overtaking car is moving relative to the static vehicles with excess speed v. This models a moving car platoon being overtaken by a single vehicle. The overtaking vehicle is sketched at a bumper to bumper distance of $d = 0$ m.

for example, in directional neighbor discovery [48], where only one link end applies beamforming. Our RX equipment is put into a static (parked) car. The RX antenna is fixed to the left rear car window. Our TX is approximately 15 m behind the RX car. Single reflections at the TX car do not occur because of the directivity of the horn antenna, while double reflections involving the TX car are below the receiver sensitivity. Hence, the TX car is omitted and replaced by a simple tripod mounting. The TX and RX placement is shown in Figs. 1 and 2.

To simplify the measurements, we do not move TX and RX, but rather keep them static, and have the overtaking car emulated by regular street traffic passing by. As indicated above, this approach is valid because interaction by houses and other static objects are negligible due to the directivity of the TX horn antenna. Due to the spatial filtering, Doppler is mainly determined by the relative velocity of the overtaking vehicle. Our case corresponds to a "moving frame of reference". Keeping TX and RX static makes a very accurate time and frequency synchronization possible. The frequency synchronization is achieved via a 10 MHz reference signal distribution to all clocks. The time synchronization is achieved with a marker signal that triggers the receiver when the sounding signal is transmitted. A measurement is triggered once the overtaking vehicle is driving through a first light barrier, positioned at d_{start}. The distance d_{start} is measured from the rear bumper of the parked receiver car. The mean velocity of the overtaking vehicle is estimated through a second light barrier, positioned 3 m after the first one. We measured the time Δt it took for the vehicle to arrive at the second light barrier. By means of the mean velocity estimate $\hat{v}$ and the starting point d_{start}, we estimate the position of the overtaking vehicle at all time points m to

$$\hat{d}[m] = \hat{v} \cdot m\, T_{\text{snap}} + d_{\text{start}} = \frac{3\,\text{m}}{\Delta t}\, m\, T_{\text{snap}} + d_{\text{start}}\,, \quad (1)$$

where T_{snap} is the snapshot rate, provided in Appendix B. We hence take the front bumper of the overtaking vehicle and the rear bumper of the parked receiver car as reference planes. The distance d is thus referred to as the "bumper to bumper distance". The range of interest is marked via meter marks on the left-hand side in Fig 1. Memory space is limiting the recording time of our 510 MHz broadband signal to 720 ms. Due to this limitation, the recorded measurements do not necessarily cover all distances of interest. To cover the distances shown in Fig. 1, the light barriers, triggering the measurements, are placed at three different positions. In other words, d_{start} is varied. An exemplary light barrier position to cover the larger distances is illustrated in Fig 1.

III. RECEIVE POWER FLUCTUATION (LARGE-SCALE FADING) DURING OVERTAKING

We have built a dedicated channel sounder for this experiment (for details see Appendix B) that provides estimates of the time-variant transfer function $H[m, q]$. The time index is denoted by $m \in \{0, \ldots, S-1\}$ and the frequency index is denoted by $q \in \{0, \ldots, K-1\}$, where $K = 103$. The time-variant CIR $h[m, n]$ with delay index n is obtained via an inverse discrete Fourier transform[3]. The CIR h exhibits a sparse structure. Therefore, the median of all samples of h is used as estimator of the noise floor [49]. All values of the CIR below a threshold that is 6 dB above this noise floor are set to zero.

Similar as in [47], we estimate the large-scale fading by applying a moving average filter of length L_{f}. Likewise, we assume that the fading process is stationary as long as the movement of the scattering object (the overtaking vehicle) is within $L_{\text{c}} \triangleq 50\,\lambda = 50 \cdot 5\,\text{mm} = 0.25\,\text{m}$. The filter length L_{f} depends on the velocity of the overtaking vehicles and is always chosen to cover L_{c} and to extend it to the earlier and later time point by $\Delta L = 10$ samples [47]. It hence

[3]We do not apply window functions so that the temporal resolution will not be degraded. This will be important for the data evaluation in Section IV.

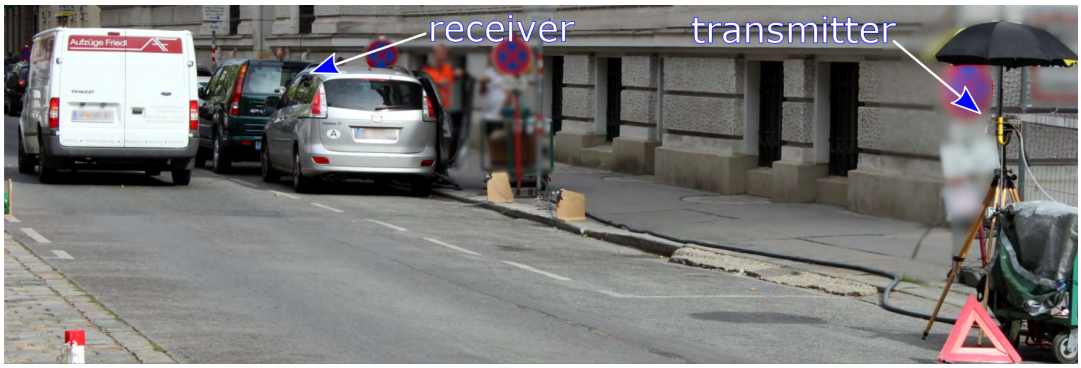

FIGURE 2. Measurement site. TX and RX are static. Urban street traffic is passing by. At this snapshot, the overtaking vehicle is at a bumper to bumper distance of approximately $d = 6$ m.

calculates to

$$L_\mathrm{f} = L_\mathrm{c} + 2\,\Delta L = \left\lfloor \frac{50\lambda}{v \cdot T_\mathrm{snap}} \right\rfloor + 2 \cdot 10\,. \tag{2}$$

The estimate of the time-varying second moment $\hat{\Omega}[m]$ is then calculated as

$$\hat{\Omega}[m] = \frac{1}{I_\mathrm{U}[m] - I_\mathrm{L}[m] + 1} \sum_{m'=I_\mathrm{L}[m]}^{I_\mathrm{U}[m]} \sum_{n=0}^{K-1} \left|h[n, m']\right|^2\,, \tag{3}$$

where the lower and the upper sum index are

$$I_\mathrm{L}[m] = \max(0, \lceil m - (L_f/2) \rceil)\,, \tag{4}$$

$$I_\mathrm{U}[m] = \min(\lceil m + (L_f/2) \rceil, S - 1)\,. \tag{5}$$

Our scenario is dominated by the LOS component. As we keep TX and RX static, this component will always appear at the same delay tap, called n_LOS. To analyze the strength of the LOS delay tap relative to all taps, we estimate the second moment of the LOS tap as well.

$$\hat{\Omega}^\mathrm{LOS}[m] = \frac{1}{I_\mathrm{U}[m] - I_\mathrm{L}[m] + 1} \sum_{m'=I_\mathrm{L}[m]}^{I_\mathrm{U}[m]} \left|h[n_\mathrm{LOS}, m']\right|^2\,. \tag{6}$$

The delay index n_LOS is calculated based on the measured TX–RX distance. Both estimates $\hat{\Omega}[m]$ and $\hat{\Omega}^\mathrm{LOS}[m]$ are parameterized by the time index m. All time-dependent quantities are equally well parameterized by the relative position estimate (1). With an abuse of notation we denote, for example,

$$\hat{\Omega}[d] = \hat{\Omega}\left[\hat{d}^{-1}[d]\right]\,. \tag{7}$$

A. STATISTICAL EVALUATION AND DISCUSSION

In this sub-section, we perform the statistical evaluation of the large-scale fading and then discuss the results. The experiment was conducted for 30 different vehicles, from which we derive ensemble statistics.

The first quantity of interest is the position-specific relative LOS tap gain, that is $\hat{\Omega}^\mathrm{LOS}[\hat{d}]/\hat{\Omega}[\hat{d}]$. This quantity is evaluated as boxplot in the top panel of Fig. 3. Our evaluation is based on a window size of $L_\mathrm{c} = 50\,\lambda = 0.25$ m length. For sake of illustration, we plot the graphs on a meter based grid by rounding $\hat{d}$ to the nearest integer meter value. In all the boxplots of our contribution, the bottom and top edges of the box indicate the 25$^\mathrm{th}$ and 75$^\mathrm{th}$ percentiles. The whiskers show the 5$^\mathrm{th}$ and 95$^\mathrm{th}$ percentiles. All observations outside the whiskers are marked with crosses. The bottom panel of Fig. 3 shows the number of samples we obtain for each meter bin. Please note that the maximum number of samples (per bin) is 120, since we observed 30 vehicles and obtain 4 samples per meter.

We observe that the LOS tap captures most of the channel gain and never drops below -4 dB. Cars (in red) and SUVs (in green) show a similar trend. For both vehicle types, the relative gain of the LOS tap increases when the overtaking car is at larger distances d. The additional MPC due to the overtaking vehicle fades out and the limiting value is reached after $d > 5$ m. Trucks show a different trend. If a truck is close to the RX, the relative gain of the LOS tap is increased, but for larger distances it approaches a lower limiting value. This is intuitively explained by strong MPCs generated at the side wall of trucks. Whenever a truck is "close enough", these MPCs are not resolved in the time domain and are binned in the LOS tap.

To further study the above mentioned side-wall wave interaction effect, we analyze the gain increase of the LOS tap versus the distance. The gain increase relative to no vehicle presence (indicated as $d \to \infty$) is plotted in the middle panel of Fig. 3. Cars and SUVs show no effect. In contrast, overtaking trucks potentially boost the LOS gain by more than 10 dB. The median result shows an increase of approximately 2 dB.

IV. SMALL-SCALE FADING OF THE LOS TAP DURING OVERTAKING

As we discussed in the section above, the LOS tap is the dominating contribution of the channel gain. Here, we are interested in the small-scale fading behavior of this LOS tap. To suppress large-scale fading effects, the channel is normalized by the square root of the estimated second moment,

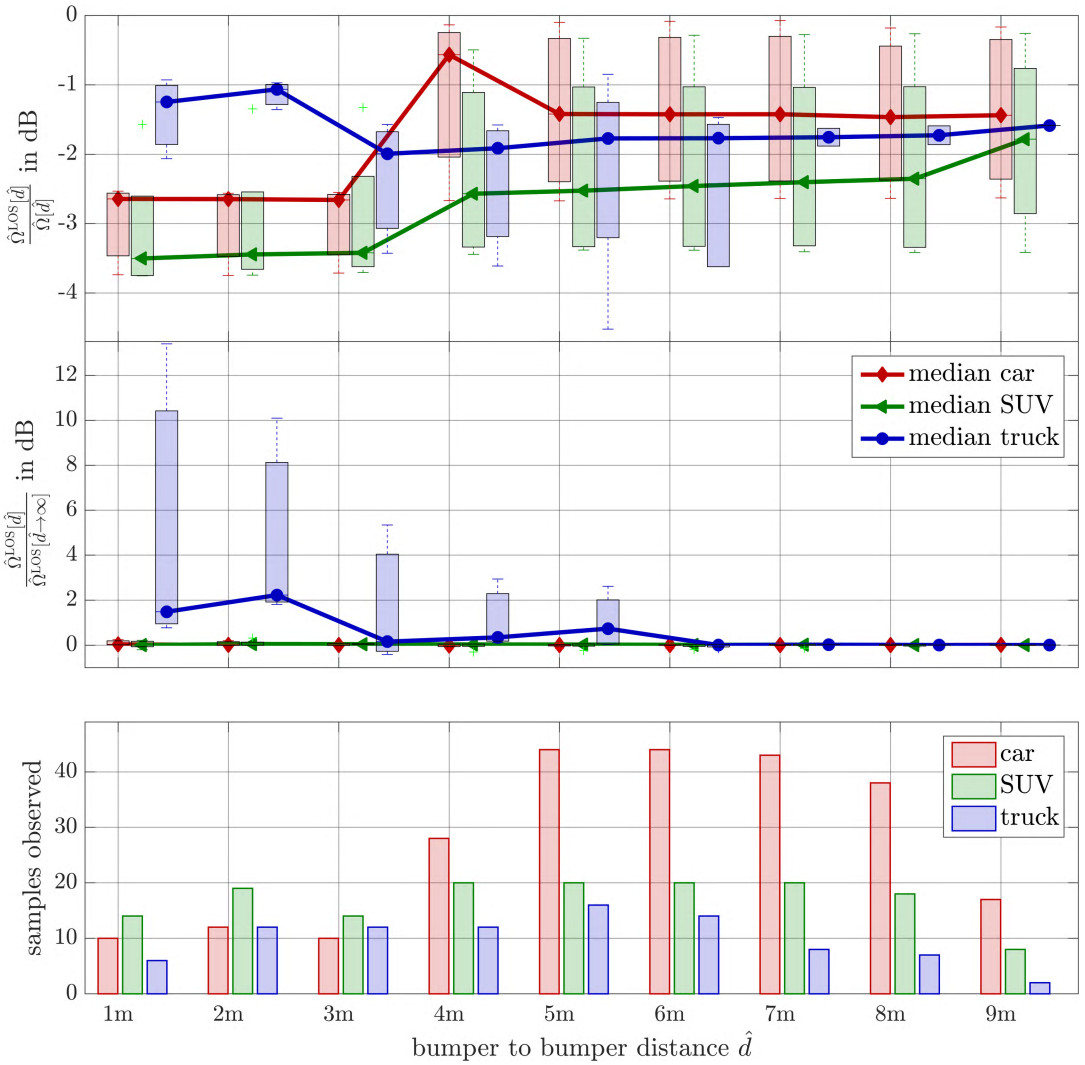

FIGURE 3. (top) Box plot of the LOS tap gain relative to the gain of all taps. When cars and SUVs are close to the RX antenna ($d = 1$ m), additional MPCs are created, thus decreasing the relative LOS gain. For trucks the converse is true because strong interactions with the side wall (scattering, diffraction) add power to the LOS tap. (middle) Box plot of the LOS tap gain increase by an overtaking vehicle compared to "no vehicle present". When cars and SUVs pass by, the LOS tap is hardly affected. The side walls of trucks strongly reflect impinging waves. (bottom) Number of samples used for the evaluation above.

that is

$$\tilde{h}[m, n_{\mathrm{LOS}}] = \frac{h[m, n_{\mathrm{LOS}}]}{\sqrt{\hat{\Omega}^{\mathrm{LOS}}[m]}}. \tag{8}$$

As a demonstrative example, we provide the channel impulse responses and estimates of the second moment for an overtaking truck, see Fig. 4 for a photograph of the truck and Fig. 5 for the LOS channel estimates. Before we study the small-scale fading statistics, we note that there is an oscillation with evolving instantaneous frequency visible in Fig. 5. The oscillations of the red curve with time-varying beating frequency can be explained by the Doppler shift changing with d, see Fig. 6 for the spectrogram[4] of $|\tilde{h}[m, n_{\mathrm{LOS}}]| - 1$.

[4]The spectrogram uses a Kaiser window of length 256 and shape parameter $\alpha = 5$. The Kaiser window approximates the discrete prolate spheroidal (DPS) sequence window [50, p. 232 ff.], that will be later extensively used for the Doppler analysis in Section V.

A. GEOMETRIC ARGUMENTATION FOR TWDP SMALL-SCALE FADING

The TWDP small-scale fading model assumes fading due to the interference of two strong radio signals and numerous smaller, so called diffuse, signals. In our case, the two strong radio signals are the unblocked LOS and a scattered component from an overtaking vehicle that arrives at the same delay tap. Our measurement bandwidth of BW = 510 MHz allows to resolve MPCs that are separated by a delay of $\Delta\tau \approx 1/\mathrm{BW} \approx 2$ ns or a travel distance of $\Delta s \approx c_0/\mathrm{BW} \approx 60$ cm. Every MPC separated less than these values is not resolved and interpreted as fading. We define the Fresnel ellipsoids for the MPCs arriving at the same time tap (bin) as the component corresponding to LOS

$$|\tau_{\mathrm{LOS}} - \tau_{\mathrm{refl}}| \leq \frac{1}{\mathrm{BW}}. \tag{9}$$

FIGURE 4. Webcam snapshot of the exemplary overtaking truck ($d \approx 5$ m).

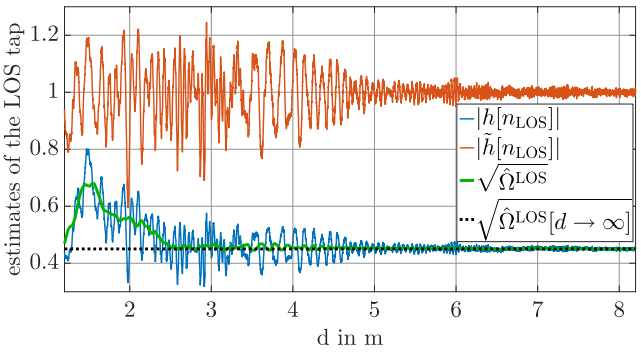

FIGURE 5. Result of the post-processing of the LOS tap for the exemplary truck shown in Fig. 4. The lower, blue curve shows the LOS channel tap $h[n_{\mathrm{LOS}}]$ including large-scale fading. The green, smooth curve shows the estimated large-scale fading $\sqrt{\hat{\Omega}^{\mathrm{LOS}}}$. The black dashed line is the estimate of the channel gain without a vehicle present. The red curve shows the normalized LOS channel tap $\tilde{h}[n_{\mathrm{LOS}}]$, that is, the small-scale fading only. The oscillatory behavior stops at approximately 5 m.

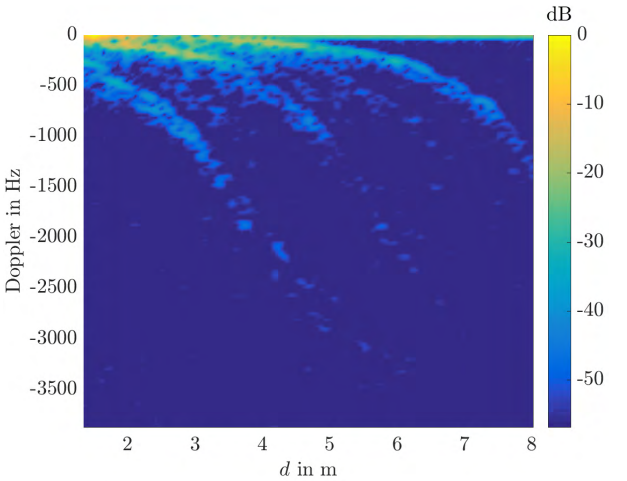

FIGURE 6. Spectrogram of the normalized LOS channel tap ($|\tilde{h}[n_{\mathrm{LOS}}]| - 1$) from Fig. 5. The oscillatory behavior is best explained by the two strong, yellow traces in the spectrogram.

In Fig. 7, this ellipse is shown in red. The green car in Fig. 7 shows the maximum distance values ($d \approx 4.5$ m) for which an overtaking car is producing TWDP fading. Figure 7 also

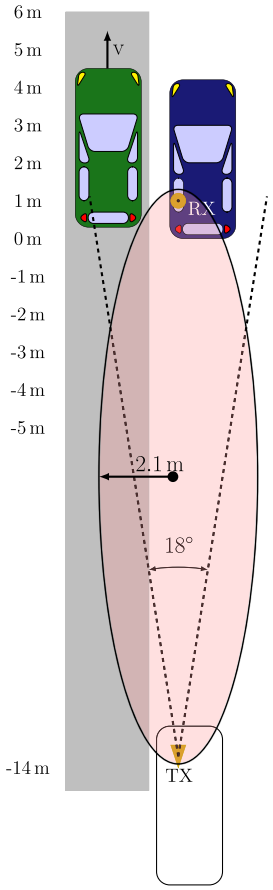

FIGURE 7. Scaled sketch (1:5000). The LOS tap fades if another object is within the red filled ellipse (semi-minor axis equals 2.1 m). The green car in this figure is sketched such that it just produces TWDP fading. If the car goes further on, its scattered component will be at the next channel tap.

shows the half power beam width of the TX horn. This illustrates that the distance region 0 . . . 4 m leads to a signal created by wave interaction with the overtaking vehicle that is not much weaker than the LOS component. Hence, we expect two MPCs at the same order of magnitude. In the region before, for example, −5 . . . 0 m the ellipsoid condition to experience TWDP fading is fulfilled but spatial filtering by the horn antenna suppresses the scattered component. By inspecting Fig. 5 again, one observes that the oscillatory behavior fades out after 5 m, as the overtaking truck is a rather short one. In the following subsection we briefly introduce the mathematics of the TWDP model. In Section IV-C, we focus on maximum likelihood estimation (MLE) of the model parameters and perform model selection to draw eventually statistical conclusions.

B. MATHEMATICAL DESCRIPTION OF TWDP FADING

TWDP fading was first introduced in [51]. A more extensive mathematical description was provided in [52]. For the convenience of the reader, we briefly summarize [52]. The TWDP fading model in the complex-valued baseband is given as

$$r_{\mathrm{complex}} = V_1 e^{j\phi_1} + V_2 e^{j\phi_2} + X + jY \,, \tag{10}$$

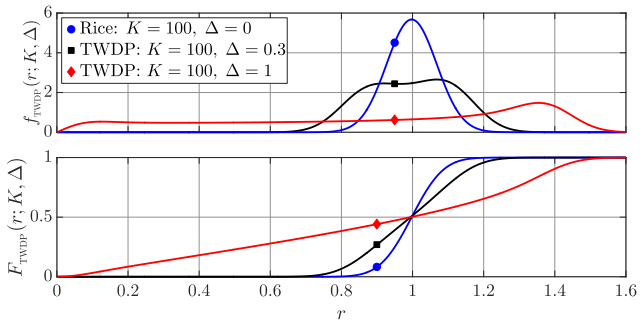

FIGURE 8. Comparison of Rician, and TWDP fading. The TWDP distribution with $\Delta = 1$ deviates strongly from the Rice distribution. Smaller Δ values do not affect the shape of the distribution as severely.

where $V_1 > 0$ and $V_2 \geq 0$ are the deterministic amplitudes of the non-fluctuating components. The phases ϕ_1 and ϕ_2 are independent and uniformly distributed in $(0, 2\pi)$. The diffuse components are modeled via the law of large numbers as $X + jY$, where $X, Y \sim \mathcal{N}(0, \sigma^2)$ are independent Gaussian random variables. The K-factor is defined analogously to the Rician K-factor as the power ratio of the non-fluctuating components and the diffuse components

$$K = \frac{V_1^2 + V_2^2}{2\sigma^2} \,. \tag{11}$$

The parameter Δ describes the amplitude relationship among the non-fluctuating components

$$\Delta = \frac{2V_1V_2}{V_1^2 + V_2^2} \,. \tag{12}$$

The Δ-parameter is bounded between 0 and 1 and equals 1 iff both amplitudes are equal. Iff $\Delta = 0$, TWDP fading degenerates to Rician fading. This transition from TWDP fading to Rician fading is smooth. If the second non-fluctuating component becomes very small, it can be absorbed equally well in the diffuse components. This is discussed in detail in Appendix C.

The cumulative distribution function (CDF) of the envelope of (10) is

$$F_{\mathrm{TWDP}}(r; K, \Delta) = 1 - \frac{1}{2\pi} \int_0^{2\pi} Q_1\left(\sqrt{2K\,[1 + \Delta\cos(\alpha)]},\ \frac{r}{\sigma}\right) \mathrm{d}\alpha \,, \tag{13}$$

where $Q_1(\cdot, \cdot)$ is the Marcum Q-function. Figure 8 shows an example of the probability density function (PDF) $f_{\mathrm{TWDP}}(r; K, \Delta)$ and CDF $F_{\mathrm{TWDP}}(r; K, \Delta)$ of the TWDP fading distribution.

C. MAXIMUM LIKELIHOOD ESTIMATION OF K AND Δ AND MODEL SELECTION

Based on the filtered envelope measurement data of the LOS delay $r[m] = \left|\tilde{h}[m, n_{\mathrm{LOS}}]\right|$, we are seeking the TWDP fading distribution of which the observed realizations appear most likely. To do so, we estimate the parameter tuple $(\hat{K}[m], \hat{\Delta}[m])$ via MLE

$$(\hat{K}[m], \hat{\Delta}[m]) = \arg\max_{K,\Delta} \sum_{m'=m-(L_{\mathrm{c}}/2)}^{m+(L_{\mathrm{c}}/2)-1} \ln f_{\mathrm{TWDP}}(r[m']; K, \Delta) \tag{14}$$

For the MLE, we take all samples within the assumed stationary length of $L_{\mathrm{c}} \triangleq 50\lambda$. The maximization is implemented as exhaustive search on a (K, Δ) grid specified in Appendix C. We also perform MLE for the Rician K-factor. To do so, we restrict the maximization (14) to the parameter tuple $(K, \Delta \equiv 0)$. Taking the data of the exemplary truck (Figs. 4 to 6), the estimated CDFs and their evolution is shown in Fig. 9. The three smallest distances (in Fig. 9) show CDFs where the truck is in proximity of the receive antenna. There we observe fading that is not well explained by a Rician fit. The proposed TWDP fading model shows a superior fit. Only the last example at a distance of 6 m clearly fades according to a Rice distribution. Of course, TWDP fits must always be better than Rician fits as the Rician model is a special case of TWDP. However, the TWDP model introduces an additional parameter, which is not desirable.

Thus, to select between Rician fading and TWDP fading, we employ Akaike's information criterion (AIC). The AIC is a rigorous way to estimate the Kullback-Leibler divergence, the relative entropy based on MLE [53]. Given the MLE fitted parameter tuple $(\hat{K}[m], \hat{\Delta}[m])$ of TWDP fading and Rician fading, we calculate the sample size N corrected AIC [53, p. 66] for Rician fading ($\Delta \equiv 0$) and TWDP fading

$$\mathrm{AIC}[m] = -2 \sum_{m'=m-(L_{\mathrm{c}}/2)}^{m+(L_{\mathrm{c}}/2)-1} \ln f_{\mathrm{TWDP}}(r[m']; \hat{K}, \hat{\Delta}) + 2U + \frac{2U(U+1)}{N - U - 1}, \tag{15}$$

where the model orders U for Rician and TWDP fading are 1 and 2, respectively. We choose between Rician fading and TWDP fading based on the lower AIC value. Due to the model order penalization in the AIC we avoid over-fitting. For our exemplary truck, the fitted parameters as well as the selected model are shown in Fig. 10.

D. STATISTICAL EVALUATION AND DISCUSSION

In this sub-section, we show the ensemble statistics of small-scale fading. Depending on the selected model, we take either the TWDP K-factor or the Rician K-factor. For Rician fits we set $\Delta \equiv 0$. Notice, however, that we rely then on the success of the model selection algorithm. Especially for very small Δ-parameters, very likely, we decide for Rician fading and hence bias the found Δ-parameters towards smaller values. This is discussed in Appendix C.

Figure 11 illustrates the fitted K-factors and Δ-parameters. The K-factor is smaller if the vehicle is closer to the RX antenna (closer to the rear bumper of the car). If the vehicle passes the static RX car, the K-factor saturates. Basically the LOS tap does not fade any longer. As mentioned above,

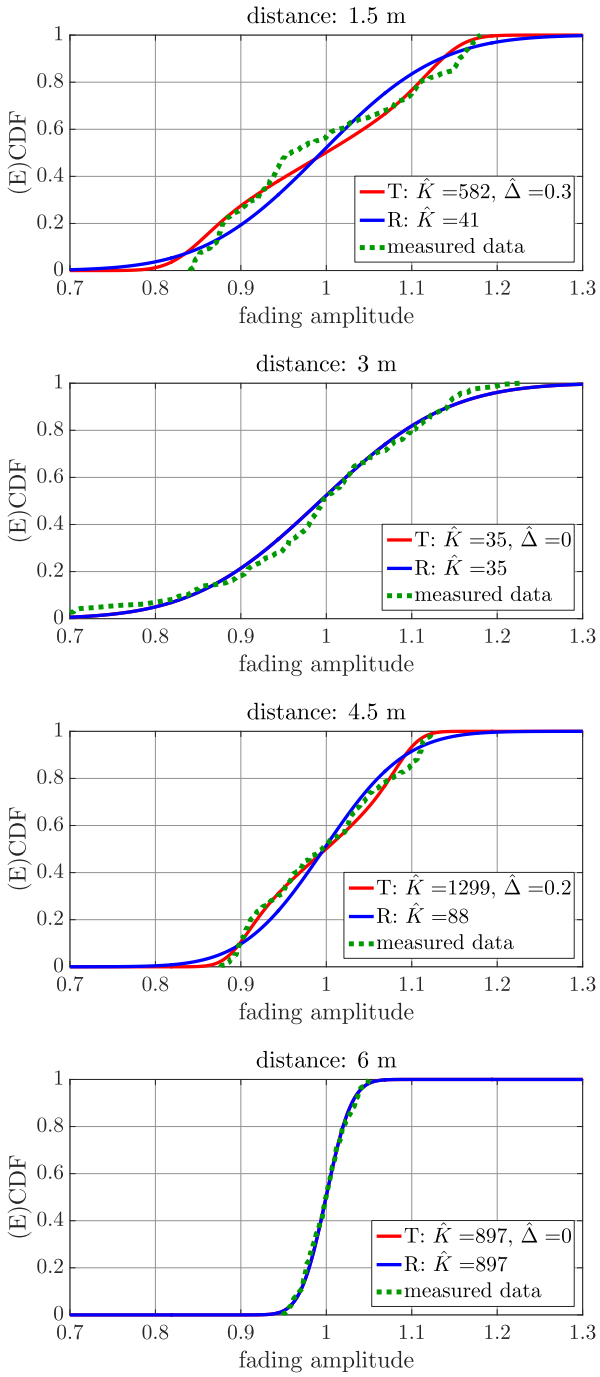

FIGURE 9. CDF evolution over distance. The data is again from our example, see Figs. 4 to 7. For distances smaller than 5 m, TWDP fading leads to a superior fit. At first glance, the Rician model seems to achieve a good fit as well, however, the K-factors of both models are not in the same order of magnitude. Rician fading underestimates the power in the non-fluctuating components.

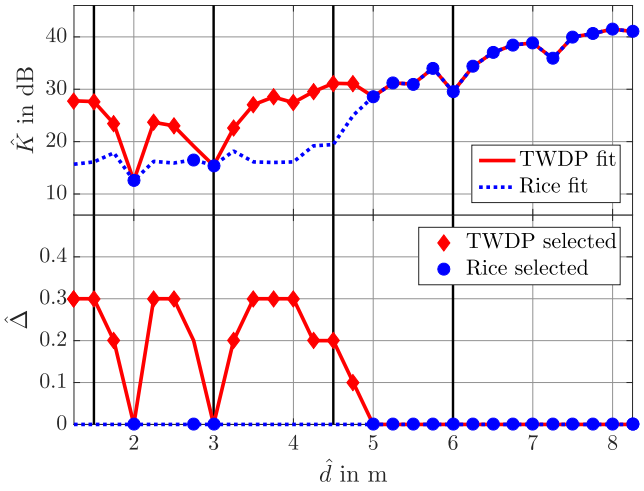

FIGURE 10. MLE fitted parameter tuple ($\hat{K}$, $\hat{\Delta}$) for the exemplary truck channel from Fig. 5. The Rician K-factor (blue dashed line) underestimates the power within the non-fluctuating components. If AIC selects TWDP fading, a red diamond marks the parameter tuple. If Rician fading is selected, a blue circle is used. The black vertical lines illustrate the positions evaluated in Fig. 9.

the vehicle size is translated to the distance d. For longer vehicles such as trucks, it takes longer until the K-factor starts rising. SUVs lie in between cars and trucks.

Next, we focus on the Δ-parameter. We see that the length of the vehicle also affects this parameter. We observe TWDP fading, that is, $\Delta > 0$, whenever a part of the vehicle is still close to the RX antenna. The longer the vehicle, the longer this effect is visible. Remember that the median Δ value has a slight negative bias, as we set Δ to zero if we decide for Rician fading. This explains why the SUV median is zero at 2 m, although the Δ values are spread out; since in case of SUVs, the AIC decides for Rician fading more than half of the time. The AIC model selection decisions are color-coded in the histogram in the bottom panel of Fig. 11. The histogram in lighter shades is identical to the histogram of Figure 3. The darker shades show the number of samples where the AIC decided for TWDP fading. Again, looking at the maximum distances where TWDP fading occurs, we see a correlation with the vehicle length.

V. DELAY-DOPPLER DISPERSION EVALUATED VIA THE LOCAL SCATTERING FUNCTION

To study the delay-Doppler dispersion of our vehicular channel, we characterize the channel by the LSF, as explained in [47], [54], and [55]. Similar to the previous sections, we assume that the fading process is locally stationary within a region of M samples in time and all samples in frequency domain. We hence estimate the LSF for consecutive stationarity regions in time. We use a multitaper based estimator in order to obtain multiple independent spectral estimates from the same measurement and being able to average them. The estimate of the LSF is defined as [54]

$$\hat{C}[k_t; n, p] = \frac{1}{IJ} \sum_{w=0}^{IJ-1} \left| \mathcal{H}^{(G_w)}[k_t; n, p] \right|^2 . \tag{16}$$

By $p \in \{-K/2, \ldots, K/2\}$ we denote the Doppler index, and as in the previous sections, we denote by $n \in \{0, \ldots, M-1\}$ the delay index. The delay and Doppler shift resolutions are given by $\tau_s = 1/(K\Delta f)$ and $\nu_s = 1/(MT_{\text{snap}})$. The time index

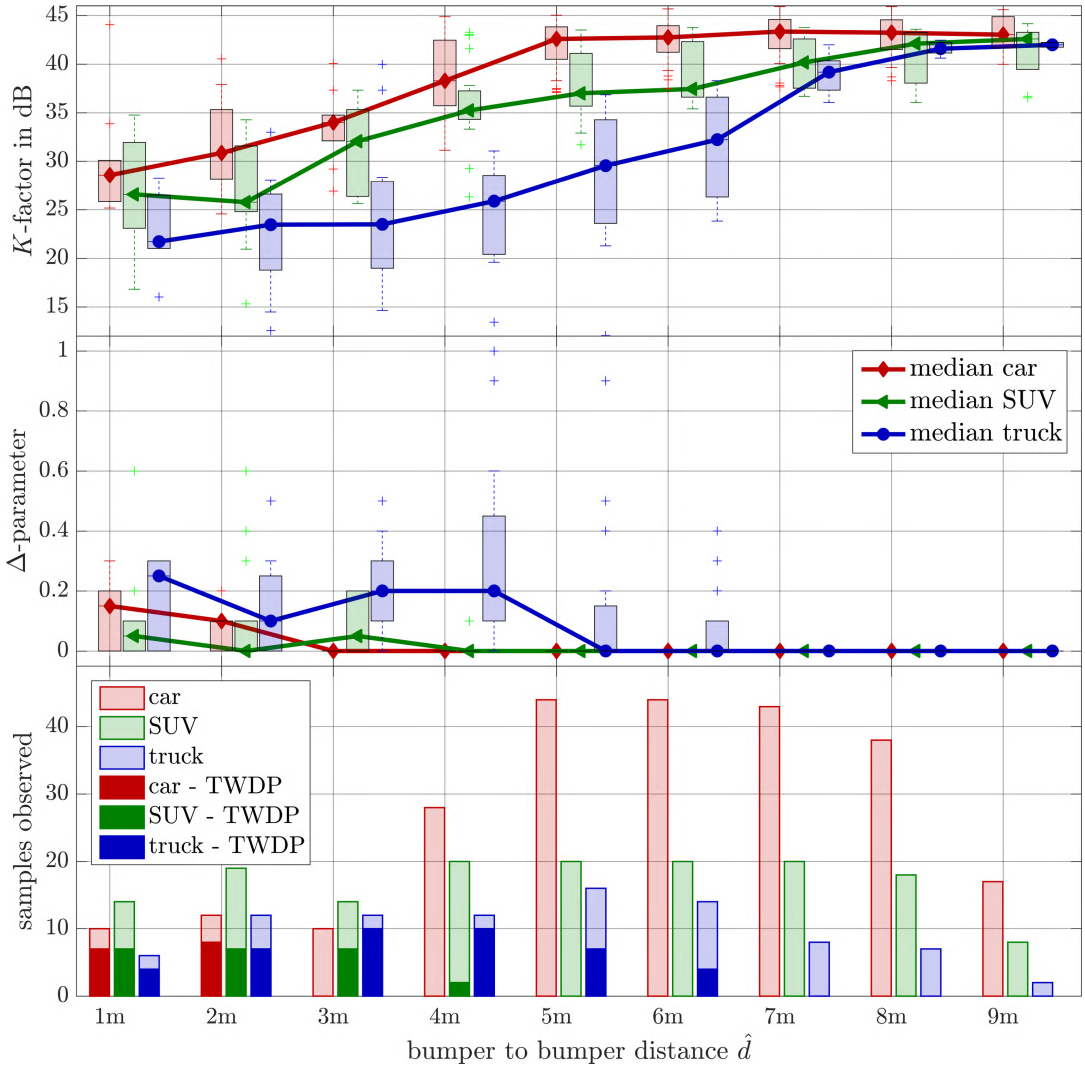

FIGURE 11. (top) Boxplot of the Rician fading and TWDP fading K-factor. The closer the vehicle to the RX and the larger the vehicle, the stronger are the diffuse components. (middle) Boxplots of the Δ-parameter. The larger the vehicle, the stronger is the second non-fluctuating component. For example, $\Delta = 0.2$ (for trucks) correponds to a second non-fluctuating component that is 20 dB smaller than the LOS component, see Fig. 15 in Appendix C. (bottom) Histogram of all samples observed and the TWDP samples. This shows the TWDP selection ratio.

of each stationarity region is $k_t \in \{0, \ldots, \lfloor (S/M - 1 \rfloor)\}$ and corresponds to the center of the stationarity regions. The windowed spreading function $\mathcal{H}^{(G_w)}$ is calculated by

$$\mathcal{H}^{(G_w)}[k_t; n, p] = \sum_{\substack{m= \\ -M/2}}^{M/2-1} \sum_{\substack{q= \\ -K/2}}^{K/2} H[m + Mk_t, q]\, G_w[m, q]\, \mathrm{e}^{-\mathrm{j}2\pi(pm - nq)}, \tag{17}$$

where the tapers $G_w[m, q]$ are the DPS sequences [56], explained in detail in [54]. The number of tapers in time domain is $I = 3$ and in frequency domain $J = 3$.

We set $M = 233$ which corresponds to a stationarity region of 30 ms in time. The power delay profile (PDP) and the Doppler spectral density (DSD) are calculated as a summation (marginalization) of the LSF over the Doppler domain or delay domain [54],

$$\mathrm{PDP}[k_t; n] = \sum_{p=-M/2}^{M/2-1} \hat{\mathcal{C}}[k_t; n, p]\ , \tag{18}$$

$$\mathrm{DSD}[k_t; p] = \sum_{n=0}^{K-1} \hat{\mathcal{C}}[k_t; n, p]\ . \tag{19}$$

Based on the PDP and DSD, we analyze the time-varying RMS delay spread and the RMS Doppler spread. To obtain these quantities, we use the formulas (10)–(13) from [54].

Our measurements were carried out in a street with 30 km/h speed limit. The average vehicle speed is in this order, but some vehicles significantly deviate from the

average speed. To compare vehicles at different speed, the Doppler profile of each vehicle is first normalized w.r.t. to its maximum Doppler shift

$$\nu_{\max} = \frac{2\hat{v}}{\lambda} \,. \tag{20}$$

Next the Doppler profile is re-scaled to a common speed of $v = 30\,\text{km/h} \approx 8.33\,\text{m/s}$. The data post-processing for our exemplary truck is shown in Fig. 12. Figure 12(a) shows the PDP as it evolves over distance. A bandwidth of 510 MHz is not sufficient to distinguish the MPCs in the time-domain. A small channel gain increase in the delay range $10 - 30\,\text{ns}$ is visible after approximately 5 m. Figure 12(c) shows the corresponding DSD. The additional MPCs from the overtaking truck are clearly visible as negative Doppler shift traces. Note that these traces are already partially demonstrated in Fig. 6. Figure 12(b) shows the respective RMS spread values.

A. STATISTICAL EVALUATION AND DISCUSSION

The results for the whole data ensemble are illustrated in Fig. 13. The bottom panel shows again the number of samples used for the evaluation at each individual position. Note, that the histogram is slightly different to the previous ones. Previously we performed the evaluation on 50λ in space, which equals 30 ms evaluation time exactly only for a vehicle at a speed of $v \approx 8.25\,\text{m/s} = 29.7\,\text{km/h}$.

The RMS delay spread, illustrated in the top panel of Fig. 13, is only slightly affected by an overtaking vehicle. There is only a total swing of 1.5 ns for the median values of the truck. If a truck is close to the RX antenna (at approx. 1 m to 2 m) it shadows the background, boosts the already dominating LOS delay and σ_τ is smallest. Cars and SUVs barely alter σ_τ. For both vehicle types the median swing is less than 1 ns. Generally, the RMS delay spread values of different vehicles are all in the same order.

The RMS Doppler spread of cars and SUVs at distances close to the antenna ($< 3\,\text{m}$) is mainly due to phase noise of our equipment. Cars show the strongest effect on σ_ν at approximately 3 m to 4 m. SUVs show their maximum a bit later at around 4 m to 5 m. At larger distances the MPC belonging to the overtaking car (SUV) fades out. Note the similarity of σ_ν for cars and SUVs after 6 m. In this region only the rear part of the vehicles is illuminated. Trucks produce an RMS Doppler spread twice as strong as cars and as SUVs. Again, due to trucks' larger extent the maximum RMS Doppler spread occurs later, at approximately 7 m.

Keep in mind, however, that due to the spatial filtering of the horn antenna combined with the existence of a strong LOS, the RMS Doppler spread is less than 12% of the maximum Doppler shift ($\sigma_\nu \leq 0.12\,\nu_{\max}$). In the median case, σ_ν is even below one-tenth of the maximum Doppler shift $\nu_{\max}$. For comparison, a Doppler shift uniformly distributed in $(-\nu_{\max}, 0)$ yields $\sigma_\nu = \nu_{\max}/\sqrt{12} \approx 0.3\,\nu_{\max}$, a Doppler shift distributed according to a half-Jakes' spectrum yields $\sigma_\nu = \nu_{\max}\sqrt{(\pi^2 - 2^2)/(2\pi)^2} \approx 0.4\,\nu_{\max}$, and a Doppler shift according to a Jakes' spectrum even $\sigma_\nu = \nu_{\max}/\sqrt{2} \approx 0.7\,\nu_{\max}$. Modeling σ_ν with these models is therefore not appropriate. The calculations of the RMS

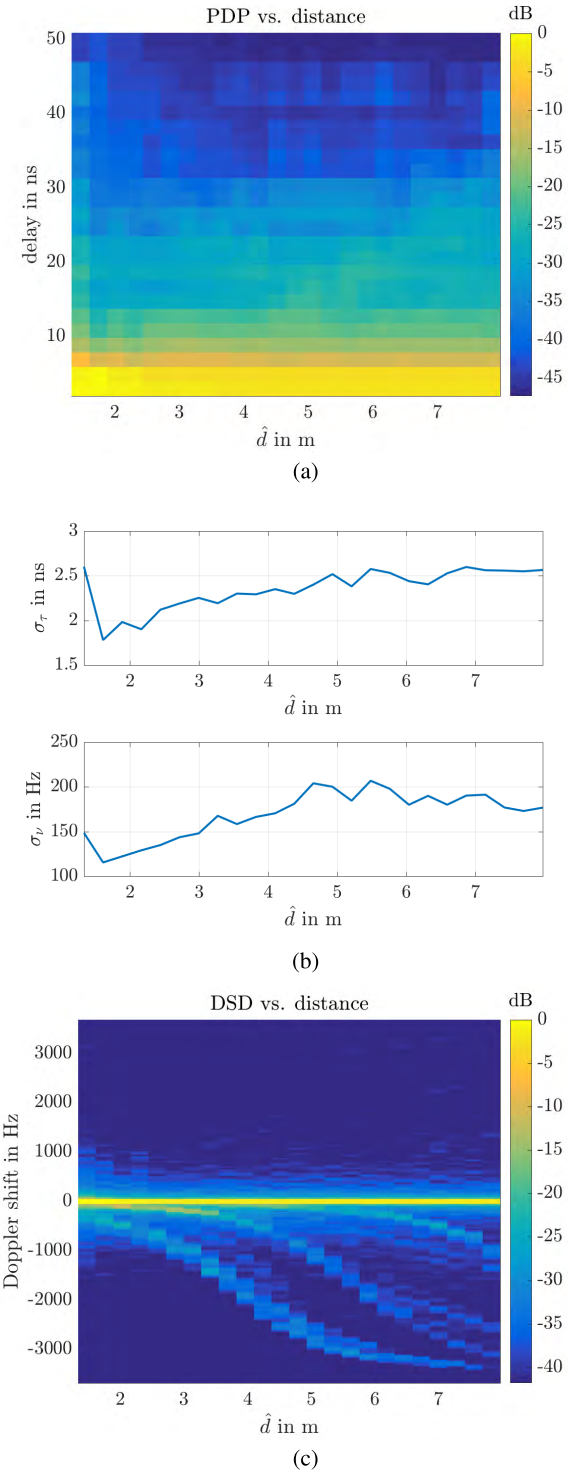

FIGURE 12. Post-processing steps to obtain the RMS delay spread and RMS Doppler spread from the LSF.(a) Time aligned PDP of the exemplary truck. The time resolution obtained with 510 MHz bandwidth is not sufficient to resolve strong MPCs. (b)Estimated RMS delay spread (top) and estimated RMS Doppler spread (bottom) are calculated on a 30 ms time grid. (c)DSD of the exemplary truck. MPC reflected at the truck are clearly visible via their Doppler shift.

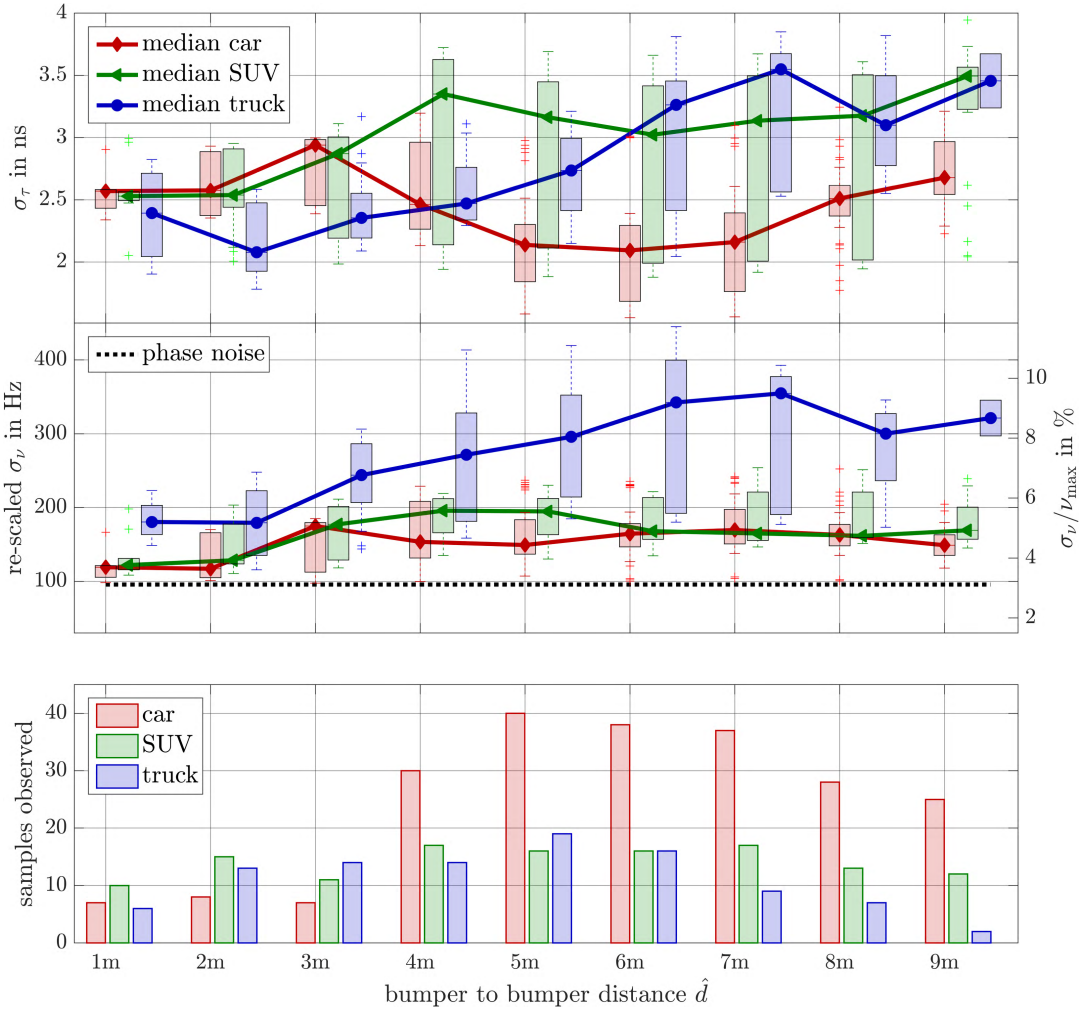

FIGURE 13. (top) Box plots of RMS delay spread as a function of bumper to bumper distance. The position of the overtaking vehicle does not have a strong impact on the RMS delay spread. (middle) Box plots of RMS Doppler spread re-scaled to a common vehicle speed of 30 km/h at the left axis. RMS Doppler spread normalized to the maximum Doppler shift is labelled at the right axis. The black dotted line shows the estimate for the RMS Doppler spread obtained through the phase noise of our measurement system. The RMS Doppler spread of cars and SUVs is only twice as much the values obtained with the phase noise only. In system without "perfect" frequency synchronization or worse reference clocks, the increase might not be visible. (bottom) Number of samples used for the evaluation above based on 30 ms sample lengths.

Doppler spread values for known distributions is provided in Appendix D.

VI. CONCLUSION

The size of the overtaking vehicle plays a crucial role for the statistics of the vehicular channel during an overtaking maneuver. Our statistical evaluation of an overtaking process has shown that large-scale fading is essentially only influenced by very large objects such as trucks and buses. Large vehicles potentially increase the receive power through scattering on their side wall by several dB. For smaller vehicles, a change of large-scale fading was not observed.

Rician fading is a good model for small-scale fading, unless a vehicle is in the "bandwidth ellipse" in which case the TWDP distribution provides a better fit. The larger the vehicle, the larger is the Δ-parameter. With the same K-factor, TWDP fading experiences deeper fades than predicted with a Rice distribution.

Furthermore, we have seen that the RMS delay spread is hardly affected by overtaking vehicles. This parameter does not need to be modeled position specific.

The analysis of Doppler dispersion has shown that the increased Doppler effect at millimeter waves is not directly translated to the RMS Doppler spread in our scenario. The RMS Doppler spread is extremely low due to spatial filtering of the horn antenna and the very strong LOS component. Only for large vehicles, this value increases significantly during overtaking. Note that the observed maximum value is a lot smaller than standard models (uniform, Jakes) would predict. The maximum observed RMS Doppler spread is approximately four times larger than the phase noise of our

measurement system. A commercial system without "perfect" frequency synchronization or worse reference clocks will very likely not experience this relatively small increase of the RMS Doppler spread at all.

APPENDIX A: ACRONYMS

AIC	Akaike's information criterion
AWG	arbitrary waveform generator
CDF	cumulative distribution function
CIR	channel impulse response
DFT	discrete Fourier transform
DPS	discrete prolate spheroidal
DSD	Doppler spectral density
LO	local oscillator
LOS	line-of-sight
LSF	local scattering function
MLE	maximum likelihood estimation
mmWave	millimeter wave
MPC	multipath component
OEW	open-ended waveguide
PDP	power delay profile
PDF	probability density function
PLL	phase-locked loop
RF	radio frequency
RMS	root mean square
RX	receiver
SA	signal analyzer
SNR	signal-to-noise ratio
SUV	sport utility vehicle
TWDP	two-wave with diffuse power
TX	transmitter
V2V	vehicle-to-vehicle

APPENDIX B: MEASUREMENT SETUP

The hardware setup is illustrated in Fig. 14. Our transmitter consists of an arbitrary waveform generator (AWG). Once triggered, it continuously repeats a baseband sounding sequence. This baseband sequence described in the following subsection is up-converted by an external mixer module. The external mixer module employs a synthesizer phase-locked loop (PLL) for generating the internal local oscillator (LO). The synthesizer PLL is fed by a 285.714 MHz reference, and uses a counter (divider) value of 210 to generate the center frequency of $f_0 = 59.99994$ GHz. Our receiver is a Rohde and Schwarz signal analyzer (SA) R&S FSW67. Its sensitivity is $P_{\mathrm{SA,min}} = -150$ dBm/Hz at 60 GHz. All radio frequency (RF) devices are synchronized with a 10 MHz reference.

When a vehicle passes the first light barrier, the AWG is triggered and plays back the baseband sequence and a sample synchronous marker signal. The marker triggers the recording of the receive samples. We directly access the IQ samples at a rate of 600 MSamples/s. From the receive IQ samples we calculate the time-variant channel transfer function $H'[m', q]$ by a discrete Fourier transform (DFT). This transforms the channel convolution into a multiplication in the frequency domain. Here m' denotes the symbol time

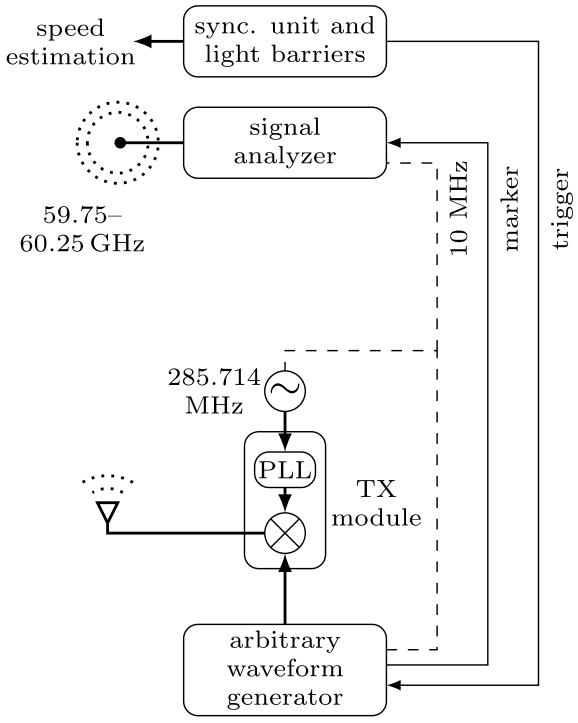

FIGURE 14. Measurement setup.

index and $q = 0, \ldots, 102$ the frequency index. After coherent averaging over N baseband symbols, we divide the resulting channel transfer function by the calibration function, obtained from back-to-back measurements, to equalize the frequency characteristics of our equipment.

EXCITATION SIGNAL

The excitation signal generated by the AWG is a multi-tone waveform. The use of a multi-tone waveform affords us several advantages such as i) ideally flat frequency spectrum, ii) design flexibility, iii) controllable crest factor, and iv) high SNR through processing gain. These advantages are important for channel transfer function extraction. Using an approach similar to a procedure implemented in [57], the excitation signal is given by $x(n) = \mathrm{Re}\left(\sum_{k=1}^{K/2} e^{j\pi \frac{k^2}{K}} e^{-j2\pi k \frac{n}{Q}}\right)$, where $n = 0, \ldots, Q-1$ is the time index and k the sub-carrier index. To minimize the crest factor of the signal, the tone phases are chosen quadratic. The crest factor is reduced in order to maximize the average transmitted power while ensuring that all RF components encountered by the excitation signals operate in their linear regions.

For the geometry of our scenario, the excess length (w.r.t. LOS length) of the MPC resulting from an overtaking car is on the order of 15 m. Ignoring multiple reflections between the parked RX car and the overtaking car, we assume that the path length difference will never be larger than 30 m. Thus, 100 ns is our maximum excess delay. To make the symbols shorter and less susceptible to inter-carrier interference caused by phase noise and Doppler, we choose the sub-carrier spacing Δf as large as possible. To still obey the sampling theorem in the frequency domain, we need to fulfil $\Delta f \leq$

$(1/(2\tau_{\max})) = 5\,\text{MHz}$, where $\tau_{\max}$ is the maximum excess delay. With our sampling rate of 600 MSamples/s this gives $Q = 121$ sub-carriers spaced by $\Delta f = 600\,\text{MHz}/121 = 4.96\,\text{MHz}$. Due to the sharp (anti-aliasing) filter of the SA, from the $Q = 121$ sub-carriers we effectively utilize only $K = 103$ sub-carriers, which is equal to a measurement bandwidth BW $\approx$ 510 MHz. With these parameters the delay resolution of the channel sounder is $\tau_{\min} = 1/\text{BW} \approx 1.96\,\text{ns}$. The receiver sensitivity is approximated to $P_{\text{RX,min}} = P_{\text{SA,min}} + 10\log_{10}(\Delta f) + 10\log_{10} K = -63\,\text{dBm}$.

LINK BUDGET AND OTHER LIMITATIONS

For the LOS component, the propagation loss including antenna gains sums up to $P_{\text{L}} = 75.5\,\text{dB}$. For the design of our setup, we assume that reflected paths are $P_{\text{R}} = 10\,\text{dB}$ weaker than the LOS component. Next, we require an SNR at each sub-carrier of the reflected component of $\text{SNR}_{\text{refl}} = 10\,\text{dB}$. These requirements directly translate to the necessary transmit power $P_{\text{TX,min}} = P_{\text{RX,min}} + P_{\text{L}} + P_{\text{R}} + \text{SNR}_{\text{refl}} = 32.5\,\text{dBm}$. The maximum power of the TX module is 7 dBm. Thus, an additional processing gain of 25.5 dB is needed. The processing gain is realized by coherently averaging over $N = \{480, 560, 640\}$ multi-tone symbols. The number of averaging symbols is chosen such that the averaged channel is still aliasing free. The least processing gain for fast vehicles ($N = 480$) is 27 dB. Remember, our multi-tone system has a sub-carrier spacing of $\Delta f = 4.96\,\text{MHz}$ and a sounding sequence length of $\tau_{\text{sym}} = 1/\Delta f = 202\,\text{ns}$. The overall pulse length including 480 repetitions, sums up to $T_{\text{snap}} = 96.8\,\mu\text{s}$. Applying the sampling theorem for the Doppler support, we obtain a maximum alias-free Doppler frequency of $\nu_{\max} = 1/(2T_{\text{snap}}) = 5.2\,\text{kHz}$, which limits the speed of overtaking cars to $v_{\text{car}} = (\lambda\nu_{\max})/2 = 12.9\,\text{m/s} = 46.5\,\text{km/h}$. This value is sufficient for our measurements, as the street, were the measurements took place, has a speed limit of 30 km/h. Our receiver is limited to a memory depth of approximately 420 MSamples or equivalently, with a sampling rate of 600 MSamples/s, we are recording $T_{\text{rec}} = 720\,\text{ms}$ of the channel evolution. At 12.9 m/s this equals a driving distance of 9.29 m. An overview of the channel sounder parameters is given in Table 1.

APPENDIX C: THE TRANSITION OF TWDP FADING TO RICIAN FADING

To study the TWDP to Rice distribution transition, we first express the Δ-parameter, defined in (12) through amplitudes, via the power ratio

$$\delta P = \frac{V_2^2}{V_1^2}\,, \quad V_2 \le V_1 \Rightarrow \delta P \le 1. \tag{21}$$

Equation (12) becomes now

$$\Delta(\delta P) = \frac{2\sqrt{\delta P}}{1+\delta P} \tag{22}$$

The expression (22) is demonstrated in Fig. 15 with δP plotted in decibels.

TABLE 1. Channel sounder parameters.

Parameter	Value
transmit antenna	20 dBi conical horn
transmit antenna heights	70, 110, 146, 156 cm
receive antenna	$\lambda/4$ monopole
receive antenna height	156 cm
transmit power	$P_{\text{TX}} = 7\,\text{dBm}$
receiver sensitivity	$P_{\text{RX,min}} = -63\,\text{dBm}$
sub-carrier spacing	$\Delta f = 4.96\,\text{MHz}$
number of sub-carriers	$K = 103$
center frequency	$f_0 = 59.99994\,\text{GHz}$
maximum alias free delay	$\tau_{\max} = 100.83\,\text{ns}$
delay resolution	$\Delta\tau = 1.96\,\text{ns}$
recording time	$T_{\text{rec}} = 720\,\text{ms}$
snapshot rate	$T_{\text{snap}} = \begin{cases} 129.1\,\mu\text{s}, & \text{if } N = 640 \\ 112.9\,\mu\text{s}, & \text{if } N = 560 \\ 96.8\,\mu\text{s}, & \text{if } N = 480 \end{cases}$
maximum car speed	$v_{\text{car}} = \begin{cases} 9.68\,\text{m/s}, & \text{if } N = 640 \\ 11.06\,\text{m/s}, & \text{if } N = 560 \\ 12.91\,\text{m/s}, & \text{if } N = 480 \end{cases}$
maximum recording distance	$d_{\max} = 9.29\,\text{m}$

For $\delta P < -20\,\text{dB}$ even an exponential power decrease is barely translated to different Δ values.

For $\Delta \to 0$, depending on the K-factor, the second much weaker component might be no longer large enough to change the distribution sufficiently from the Rician distribution. Mathematically this is expressed through the variance of the diffuse components. Given that $\Omega \equiv 1$, σ solely depends on the K-factor [58]

$$\sigma^2 = \frac{1}{2(1+K)}\,. \tag{23}$$

For $K \gg 0$, the power of the diffuse components (in decibels) is

$$20\log_{10}\sigma \approx -10\log_{10} K - 3\,\text{dB}\,. \tag{24}$$

Hence, TWDP fading differs from Rician fading only if $10\log_{10}\delta P \gg -10\log_{10} K - 3\,\text{dB}$, otherwise the second non-fluctuating component appears as strong as the diffuse components.

This behavior directly translates to the model selection algorithm. To demonstrate this, we run Monte Carlo simulations with synthetic data. Our test data is generated equivalently to the search grid used for MLE. The K-factor is linearly spaced in $\{0, 1, \ldots, 100\}$ and logarithmically spaced with 150 points for each decade above $K = 100$. The Δ-parameter is linearly spaced in $\{0, 0.1, \ldots, 1\}$. We generate 300 realizations of each pair (K, Δ) and perform the fitting and selection approach of subsection IV-C. A success is defined whenever AIC decides correctly for the TWDP model. The success rate of TWDP selection is plotted in Fig. 16. We plotted on top (as red dashed line) the relationship (22). From the considerations above, we already know that the K-factor must be at least above 3 dB. Observe that the transition region matches fairly well with those values, where the power of the second non-fluctuating component

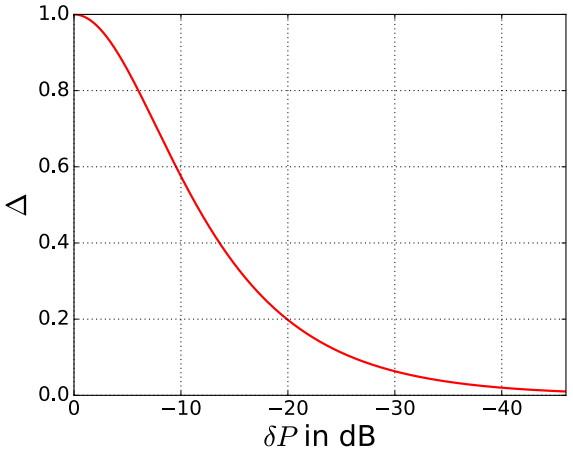

FIGURE 15. The Δ-parameter as a function of the power ratio δP of both non-fluctuating waves.

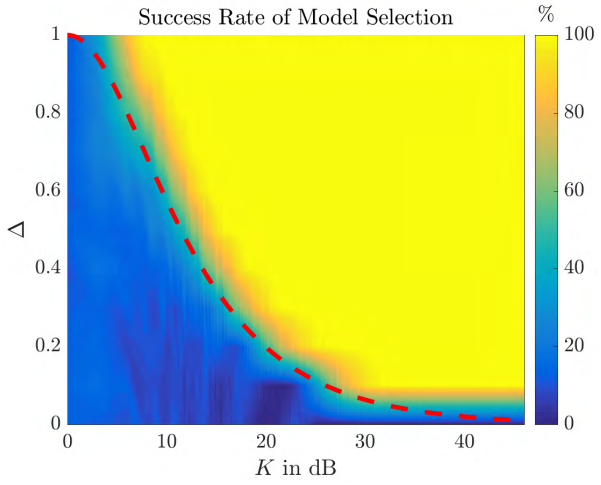

FIGURE 16. Success rate of selecting TWDP fading for all parameter tuples (K, Δ) of the grid search space. Whenever the second non-fluctuating component is in the order of the diffuse components, the AIC model selection fails. The red dashed line replaces δP of (22) with ($1/K$) to show this border.

becomes as strong at the diffuse components. However, there is a minimum $\Delta \approx 0.1$ where TWDP fading selection fails even for $K \to \infty$. From Fig. 15 we read that this value corresponds to a power difference of the LOS component and the reflected component of approximately 25 dB. With the proposed approach we are hence not capable of selecting the appropriate fading distribution for smaller, weak-reflecting vehicles. The found Δ-parameter for the statistical analysis in Subsection IV-D is therefore biased towards lower values.

APPENDIX D: RMS DOPPLER SPREAD OF KNOWN DISTRIBUTIONS

In this appendix, we derive the normalized RMS Doppler spread values σ_ν for known Doppler distributions. This yields a reference for our statistical analysis.

UNIFORM DISTRIBUTION (- LEFT SIDE)

Based on 3D uniform scattering the Doppler spectrum becomes a symmetric uniform distribution. This is simply the left half of it. Hence, the Doppler is uniformly distributed within $(-\nu_{\max}, 0)$.

$$\sigma_\nu^2 = \int_{-\nu_{\max}}^{0} \frac{1}{\nu_{\max}} \nu^2 \mathrm{d}\nu - \bar{\nu}^2 = \frac{\nu_{\max}^2}{12} \tag{25}$$

$$\boxed{\frac{\sigma_\nu}{\nu_{\max}} = \frac{1}{\sqrt{12}} = \frac{1}{2\sqrt{3}} \approx 0.2887} \tag{26}$$

JAKES' SPECTRUM

This assumes that the angle of arrival is uniformly distributed (in a plane). Through the non-linear cosine relationship between the angle of arrival and the Doppler shift, the Doppler spectrum becomes the "double horn"

$$P(\nu) = \frac{1}{\pi \sqrt{\nu_{\max}^2 - \nu^2}}\,. \tag{27}$$

The RMS Doppler spread is

$$\sigma_\nu^2 = \frac{1}{\pi\,\nu_{\max}} \int_{-\nu_{\max}}^{\nu_{\max}} \frac{1}{\sqrt{1-\left(\frac{\nu}{\nu_{\max}}\right)^2}} \nu^2 \mathrm{d}\nu = \frac{\nu_{\max}^2}{2}. \tag{28}$$

$$\boxed{\frac{\sigma_\nu}{\nu_{\max}} = \frac{1}{\sqrt{2}} \approx 0.7071} \tag{29}$$

HALF JAKES' (- LEFT SIDE)

The half Jakes' distribution sets all positive Doppler shift to zero. Here, we re-use the result from above. We only need to calculate the mean of a half Jakes' distribution.

$$\bar{\nu} = \frac{1}{\pi\,\nu_{\max}} \int_{-\nu_{\max}}^{\nu_{\max}} \frac{1}{\sqrt{1-\left(\frac{\nu}{\nu_{\max}}\right)^2}} \nu \mathrm{d}\nu = -\frac{\nu_{\max}}{\pi} \tag{30}$$

Reusing the result from above, the 2nd moment of the half-Jakes is $\frac{\nu_{\max}^2}{2} \cdot \frac{1}{2}$. Hence,

$$\sigma_\nu^2 = \frac{\nu_{\max}^2}{4} - \bar{\nu}^2 = \nu_{\max}^2 \frac{\pi^2 - 2^2}{(2\pi)^2} \tag{31}$$

$$\boxed{\frac{\sigma_\nu}{\nu_{\max}} = \sqrt{\frac{\pi^2 - 2^2}{(2\pi)^2}} \approx 0.3856} \tag{32}$$

ACKNOWLEDGMENT

This paper was presented at the Proceedings of the 12th European Conference on Antennas and Propagation, 2018 [1] and at the Proceedings of IEEE-APS Topical Conference on Antennas and Propagation in Wireless Communications, 2018 [2].

REFERENCES

[1] E. Zöchmann *et al.*, "Measured delay and Doppler profiles of overtaking vehicles at 60 GHz," in *Proc. 12th Eur. Conf. Antennas Propag. (EuCAP)*, 2018, pp. 1–5.

[2] E. Zöchmann *et al.*, "Statistical evaluation of delay and Doppler spread in 60 GHz vehicle-to-vehicle channels during overtaking," in *Proc. IEEE-APS Top. Conf. Antennas Propag. Wireless Commun. (APWC)*, Sep. 2018, pp. 1–4.

[3] T. Tokumitsu, M. Kubota, K. Sakai, and T. Kawai, "Application of GaAs device technology to millimeter-waves," *SEI Tech. Rev.*, no. 79, pp. 57–65, Oct. 2014.

[4] J. Choi, V. Va, N. González-Prelcic, R. Daniels, C. R. Bhat, and R. W. Heath, Jr., "Millimeter-wave vehicular communication to support massive automotive sensing," *IEEE Commun. Mag.*, vol. 54, no. 12, pp. 160–167, Dec. 2016.

[5] V. Va, J. Choi, and R. W. Heath, Jr., "The impact of beamwidth on temporal channel variation in vehicular channels and its implications," *IEEE Trans. Veh. Technol.*, vol. 66, no. 6, pp. 5014–5029, Jun. 2017.

[6] J. Lorca, M. Hunukumbure, and Y. Wang, "On overcoming the impact of Doppler spectrum in millimeter-wave V2I communications," in *Proc. IEEE Globecom Workshops (GC Wkshps)*, Dec. 2017, pp. 1–6.

[7] P. L. C. Cheong, "Multipath component estimation for indoor radio channels," in *Proc. IEEE Global Telecommun. Conf. (GLOBECOM)*, vol. 2, Nov. 1996, pp. 1177–1181.

[8] F. J. Velez, L. M. Correia, and J. M. Brázio, "Frequency reuse and system capacity in mobile broadband systems: Comparison between the 40 and 60 GHz bands," *Wireless Pers. Commun.*, vol. 19, no. 1, pp. 1–24, 2001.

[9] A. G. Siamarou, "Wideband propagation measurements and channel implications for indoor broadband wireless local area networks at the 60 GHz band," *Wireless Pers. Commun.*, vol. 27, no. 1, pp. 89–98, 2003.

[10] C. R. Anderson and T. S. Rappaport, "In-building wideband partition loss measurements at 2.5 and 60 GHz," *IEEE Trans. Wireless Commun.*, vol. 3, no. 3, pp. 922–928, May 2004.

[11] F. J. Velez, M. Dinis, and J. Fernandes, "Mobile broadband systems: Research and visions," *IEEE Veh. Technol. Soc. News*, vol. 52, no. 2, pp. 4–12, May 2005.

[12] N. Moraitis and P. Constantinou, "Measurements and characterization of wideband indoor radio channel at 60 GHz," *IEEE Trans. Wireless Commun.*, vol. 5, no. 4, pp. 880–889, Apr. 2006.

[13] S. Ranvier, J. Kivinen, and P. Vainikainen, "Millimeter-wave MIMO radio channel sounder," *IEEE Trans. Instrum. Meas.*, vol. 56, no. 3, pp. 1018–1024, Jun. 2007.

[14] S. Geng, J. Kivinen, X. Zhao, and P. Vainikainen, "Millimeter-wave propagation channel characterization for short-range wireless communications," *IEEE Trans. Veh. Technol.*, vol. 58, no. 1, pp. 3–13, Jan. 2009.

[15] P. F. M. Smulders, "Statistical characterization of 60-GHz indoor radio channels," *IEEE Trans. Antennas Propag.*, vol. 57, no. 10, pp. 2820–2829, Oct. 2009.

[16] K. Haneda, C. Gustafson, and S. Wyne, "60 GHz spatial radio transmission: Multiplexing or beamforming?" *IEEE Trans. Antennas Propag.*, vol. 61, no. 11, pp. 5735–5743, Nov. 2013.

[17] C. Gustafson, K. Haneda, S. Wyne, and F. Tufvesson, "On mm-wave multipath clustering and channel modeling," *IEEE Trans. Antennas Propag.*, vol. 62, no. 3, pp. 1445–1455, Mar. 2014.

[18] S. Salous, S. M. Feeney, X. Raimundo, and A. A. Cheema, "Wideband MIMO channel sounder for radio measurements in the 60 GHz band," *IEEE Trans. Wireless Commun.*, vol. 15, no. 4, pp. 2825–2832, Apr. 2016.

[19] J. Lee, J. Liang, M.-D. Kim, J.-J. Park, B. Park, and H. K. Chung, "Measurement-based propagation channel characteristics for millimeter-wave 5G Giga communication systems," *Electron. Telecommun. Res. Inst. J.*, vol. 38, no. 6, pp. 1031–1041, 2016.

[20] J. Vehmas, J. Jarvelainen, S. Le Hong Nguyen, R. Naderpour, and K. Haneda, "Millimeter-wave channel characterization at Helsinki airport in the 15, 28, and 60 GHz bands," in *Proc. IEEE 84th Veh. Technol. Conf. (VTC-Fall)*, Sep. 2016, pp. 1–5.

[21] E. Zöchmann, M. Lerch, S. Caban, R. Langwieser, C. F. Mecklenbräuker, and M. Rupp, "Directional evaluation of receive power, Rician K-factor and RMS delay spread obtained from power measurements of 60 GHz indoor channels," in *Proc. IEEE-APS Top. Conf. Antennas Propag. Wireless Commun. (APWC)*, Sep. 2016, pp. 246–249.

[22] G. R. MacCartney and T. S. Rappaport, "A flexible millimeter-wave channel sounder with absolute timing," *IEEE J. Sel. Areas Commun.*, vol. 35, no. 6, pp. 1402–1418, Jun. 2017.

[23] J. Ko *et al.*, "Millimeter-wave channel measurements and analysis for statistical spatial channel model in in-building and urban environments at 28 GHz," *IEEE Trans. Wireless Commun.*, vol. 16, no. 9, pp. 5853–5868, Sep. 2017.

[24] D. Dupleich *et al.*, "Influence of system aspects on fading at mm-waves," *IET Microw., Antennas Propag.*, vol. 12, no. 4, pp. 516–524, 2018.

[25] F. Fuschini *et al.*, "Analysis of in-room mm-Wave propagation: Directional channel measurements and ray tracing simulations," *J. Infr., Millim., Terahertz Waves*, vol. 38, no. 6, pp. 727–744, 2017.

[26] X. Wu *et al.*, "60-GHz millimeter-wave channel measurements and modeling for indoor office environments," *IEEE Trans. Antennas Propag.*, vol. 65, no. 4, pp. 1912–1924, Apr. 2017.

[27] B. Ai *et al.*, "On indoor millimeter wave massive MIMO channels: Measurement and simulation," *IEEE J. Sel. Areas Commun.*, vol. 35, no. 7, pp. 1678–1690, Jul. 2017.

[28] E. Zöchmann, M. Lerch, S. Pratschner, R. Nissel, S. Caban, and M. Rupp, "Associating spatial information to directional millimeter wave channel measurements," in *Proc. IEEE 86th Veh. Technol. Conf. (VTC-Fall)*, Sep. 2017, pp. 1–5.

[29] J. Blumenstein *et al.*, "In-vehicle channel measurement, characterization, and spatial consistency comparison of 30–11 GHz and 55–65 GHz frequency bands," *IEEE Trans. Veh. Technol.*, vol. 66, no. 5, pp. 3526–3537, May 2017.

[30] A. Chandra *et al.*, "Frequency-domain in-vehicle UWB channel modeling," *IEEE Trans. Veh. Technol.*, vol. 65, no. 6, pp. 3929–3940, Jun. 2016.

[31] P. B. Papazian, C. Gentile, K. A. Remley, and N. Golmie, "A radio channel sounder for mobile millimeter-wave communications: System implementation and measurement assessment," *IEEE Trans. Microw. Theory Techn.*, vol. 64, no. 9, pp. 2924–2932, Sep. 2016.

[32] E. Zöchmann, S. Caban, M. Lerch, and M. Rupp, "Resolving the angular profile of 60 GHz wireless channels by delay-Doppler measurements," in *Proc. IEEE Sensor Array Multichannel Signal Process. Workshop (SAM)*, Jul. 2016, pp. 1–5.

[33] C. U. Bas *et al.* (2018). "Real-time Millimeter-Wave MIMO channel sounder for dynamic directional measurements." [Online]. Available: https://arxiv.org/abs/1807.11921

[34] C. U. Bas *et al.*, "Dynamic double directional propagation channel measurements at 28 GHz—Invited paper," in *Proc. IEEE 87th Veh. Technol. Conf. (VTC Spring)*, Jun. 2018, pp. 1–6.

[35] H. Meinel and A. Plattner, "Millimetre-wave propagation along railway lines," *IEE Proc. F Commun., Radar Signal Process.*, vol. 130, no. 7, pp. 688–694, Dec. 1983.

[36] A. Kato, K. Sato, M. Fujise, and S. Kawakami, "Propagation characteristics of 60-GHz millimeter waves for ITS inter-vehicle communications," *IEICE Trans. Commun.*, vol. 84, no. 9, pp. 2530–2539, 2001.

[37] S. Takahashi, A. Kato, K. Sato, and M. Fujise, "Distance dependence of path loss for millimeter wave inter-vehicle communications," *Radioengineering*, vol. 13, no. 4, pp. 8–13, 2004.

[38] A. Yamamoto, K. Ogawa, T. Horimatsu, A. Kato, and M. Fujise, "Path-loss prediction models for intervehicle communication at 60 GHz," *IEEE Trans. Veh. Technol.*, vol. 57, no. 1, pp. 65–78, Jan. 2008.

[39] T. S. Rappaport, J. N. Murdock, and F. Gutierrez, Jr., "State of the art in 60-GHz integrated circuits and systems for wireless communications," *Proc. IEEE*, vol. 99, no. 8, pp. 1390–1436, Aug. 2011.

[40] V. Va, T. Shimizu, G. Bansal, and R. W. Heath, Jr., "Millimeter wave vehicular communications: A survey," *Found. Trends Netw.*, vol. 10, no. 1, pp. 1–113, Jun. 2016.

[41] P. Kumari, J. Choi, N. González-Prelcic, and R. W. Heath, Jr., "IEEE 802.11ad-based radar: An approach to joint vehicular communication-radar system," *IEEE Trans. Veh. Technol.*, vol. 67, no. 4, pp. 3012–3027, Apr. 2018.

[42] M. G. Sánchez, M. P. Táboas, and E. L. Cid, "Millimeter wave radio channel characterization for 5G vehicle-to-vehicle communications," *Measurement*, vol. 95, pp. 223–229, Jan. 2017.

[43] H. Wang, X. Yin, X. Cai, H. Wang, Z. Yu, and J. Lee, "Fading characterization of 73 GHz millimeter-wave V2V channel based on real measurements," in *Proc. 13th Int. Workshop Commun. Technol. Vehicles, Nets4Cars/Nets4Trains/Nets4Aircraft*, Madrid, Spain, May 2018, pp. 159–168.

[44] A. Prokes, J. Vychodil, M. Pospisil, J. Blumenstein, T. Mikulasek, and A. Chandra, "Time-domain nonstationary intra-car channel measurement in 60 GHz band," in *Proc. Int. Conf. Adv. Technol. Commun. (ATC)*, 2016, pp. 1–6.

[45] J. Blumenstein, A. Prokes, J. Vychodil, M. Pospisil, and T. Mikulasek, "Time-varying K factor of the mm-Wave vehicular channel: Velocity, vibrations and the road quality influence," in *Proc. IEEE 28th Annu. Int. Symp. Pers., Indoor, Mobile Radio Commun. (PIMRC)*, Oct. 2017, pp. 1–5.
[46] A. Loch, A. Asadi, G. H. Sim, J. Widmer, and M. Hollick, "mm-Wave on wheels: Practical 60 GHz vehicular communication without beam training," in *Proc. 9th Int. Conf. Commun. Syst. Netw. (COMSNETS)*, 2017, pp. 1–8.
[47] L. Bernadó, T. Zemen, F. Tufvesson, A. F. Molisch, and C. F. Mecklenbräuker, "Time-and frequency-varying K-factor of non-stationary vehicular channels for safety-relevant scenarios," *IEEE Trans. Intell. Transp. Syst.*, vol. 16, no. 2, pp. 1007–1017, Apr. 2015.
[48] R. Ramanathan, J. Redi, C. Santivanez, D. Wiggins, and S. Polit, "Ad hoc networking with directional antennas: A complete system solution," *IEEE J. Sel. Areas Commun.*, vol. 23, no. 3, pp. 496–506, Mar. 2005.
[49] E. S. Sousa, V. M. Jovanovic, and C. Daigneault, "Delay spread measurements for the digital cellular channel in Toronto," *IEEE Trans. Veh. Technol.*, vol. 43, no. 4, pp. 837–847, Nov. 1994.
[50] F. F. Kuo and J. F. Kaiser, *System Analysis By Digital Computer*. New York, NY, USA: Wiley, 1966.
[51] G. D. Durgin, T. S. Rappaport, and D. A. de Wolf, "New analytical models and probability density functions for fading in wireless communications," *IEEE Trans. Commun.*, vol. 50, no. 6, pp. 1005–1015, Jun. 2002.
[52] M. Rao, F. J. Lopez-Martinez, M.-S. Alouini, and A. Goldsmith, "MGF approach to the analysis of generalized two-ray fading models," *IEEE Trans. Wireless Commun.*, vol. 14, no. 5, pp. 2548–2561, May 2015.
[53] K. P. Burnham and D. R. Anderson, *Model Selection and Multimodel Inference: A Practical Information-Theoretic Approach*. New York, NY, USA: Springer, 2003.
[54] L. Bernadó, T. Zemen, F. Tufvesson, A. F. Molisch, and C. F. Mecklenbräuker, "Delay and Doppler spreads of nonstationary vehicular channels for safety-relevant scenarios," *IEEE Trans. Veh. Technol.*, vol. 63, no. 1, pp. 82–93, Jan. 2014.
[55] D. J. Thomson, "Spectrum estimation and harmonic analysis," *Proc. IEEE*, vol. 70, no. 9, pp. 1055–1096, Sep. 1982.
[56] D. Slepian, "Prolate spheroidal wave functions, Fourier analysis, and uncertainty—V: The discrete case," *Bell Syst. Tech. J.*, vol. 57, no. 5, pp. 1371–1430, May/Jun. 1978.
[57] S. Sangodoyin, J. Salmi, S. Niranjayan, and A. F. Molisch, "Real-time ultrawideband MIMO channel sounding," in *Proc. 6th Eur. Conf. Antennas Propag. (EUCAP)*, 2012, pp. 2303–2307.
[58] D. Kim, H. Lee, and J. Kang, "Comments on "Near-body shadowing analysis at 60 GHz,""*IEEE Trans. Antennas Propag.*, vol. 65, no. 6, p. 3314, Jun. 2017.

ERICH ZÖCHMANN (M'18) received the B.Sc. and Dipl.Ing. (M.Sc.) degrees (Hons.) in electrical engineering from TU Wien, in 2013 and 2015, respectively. From 2013 to 2015, he was a Project Assistant with the Institute of Telecommunications, where he co-developed the Vienna LTE-A uplink link level simulator and conducted research on physical layer signal processing for 4G mobile communication systems. From 2017 to 2018, he was a Visiting Scholar with The University of Texas at Austin. His current interests include experimental characterization and modeling of millimeter-wave propagation, physical layer signal processing, array signal processing, compressed sensing, and convex optimization.

MARKUS HOFER received the Dipl.Ing. degree (Hons.) in telecommunications from TU Wien, in 2013. He is currently pursuing the Ph.D. degree in telecommunications. From 2013 to 2015, he was a Researcher with the Telecommunications Research Center Vienna (FTW), Signal and Information Processing Department. Since 2015, he has been a Junior Scientist with the Research Group for Ultra-Reliable Wireless Machine-to-Machine Communications, AIT Austrian Institute of Technology. His research interests include low-latency wireless communications, vehicular channel measurements, modeling and emulation, time-variant channel estimation, mmwave, massive MIMO, cooperative communication systems, and interference management.

MARTIN LERCH received the master's degree in electrical engineering from TU Wien, where he is currently with the Institute of Telecommunications, developing test beds and measurement methodologies for controlled and reproducible wireless experiments at high velocities.

STEFAN PRATSCHNER was born in Vienna, Austria, in 1990. He received the B.Sc. degree in electrical engineering and the M.Sc. degree (Hons.) in telecommunications from TU Wien, in 2014 and 2016, respectively, where he is currently pursuing the Ph.D. degree with a main focus on massive MIMO technologies for mobile communications. Since 2013, he has been a Project Assistant with the Institute of Telecommunications, TU Wien.

LAURA BERNADÓ received the M.Sc. degree in telecommunications engineering from the Technical University of Catalonia (UPC), Spain, in 2007, and the Ph.D. degree from TU Wien, in 2012. She is currently a Scientist with the Austrian Institute of Technology. Her research interests include the characterization and modeling of fast time-varying and non-stationary fading processes for ultra-reliable and low-latency communications for future radio communication systems.

JIRI BLUMENSTEIN (M'17) received the Ph.D. degree from the Brno University of Technology, in 2013. In 2011, he was a Researcher with the Institute of Telecommunications, TU Wien. He has cooperated with several companies, including Racom, Volkswagen, and ON Semiconductor in the area of applied research of wireless systems and in the area of the fundamental research funded by the Czech Science Foundation. He is currently a Researcher with the Department of Radio Electronics, Brno University of Technology. His research interests include signal processing, physical layer of communication systems, channel characterization and modeling, and wireless system design.

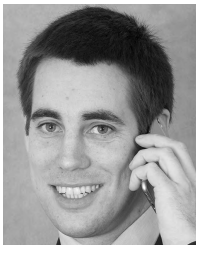

SEBASTIAN CABAN received the master's degree in business administration from the University of Vienna, Vienna, Austria, and the master's and Ph.D. degrees in telecommunications from TU Wien. His current research interest includes measurements in wireless communications.

SEUN SANGODOYIN received the B.Sc. degree in electrical engineering from Oklahoma State University, in 2007, and the M.Sc. and Ph.D. degrees in electrical engineering from the University of Southern California, in 2009 and 2018, respectively. He is currently a Postdoctoral Research Fellow with the Georgia Institute of Technology. His research interests include millimeter-wave (measurement-based) MIMO channel modeling and analysis, terahertz communications, UWB MIMO radar, parameter estimation, body area networks, and stochastic dynamical systems.

HERBERT GROLL received the B.Sc. and Dipl.Ing. (M.Sc.) degrees in electrical engineering from TU Wien, in 2014 and 2017, respectively, where he is currently pursuing the Ph.D. degree, under the supervision of Prof. C. Mecklenbräuker. His research interest includes vehicular wireless communication with an emphasis on millimeter-wave propagation for future wireless systems.

THOMAS ZEMEN was with FTW Forschungszentrum Telekommunikation Wien, Austria, and Siemens, Austria. He is currently a Senior Scientist with the AIT Austrian Institute of Technology, where he is also leading the Reliable Wireless Communications Group. He is also an External Lecturer with TU Wien. He has authored four books chapters, 37 journal papers, more than 110 conference communications, as well as two patents. His research interests include wireless ultra-reliable low-latency communications, massive MIMO systems, time-variant channel measurements, modeling and real-time emulation, as well as software-defined radio rapid prototyping. He has served as an Editor for the IEEE TRANSACTIONS ON WIRELESS COMMUNICATIONS, from 2011 to 2017.

ALEŠ PROKEŠ received the M.Sc., Ph.D., and the Habilitation degrees from the Brno University of Technology (BUT), in 1988, 1999, and 2006, respectively. Since 1990, he has been with the Faculty of Electrical Engineering and Communication, BUT, where he is currently a Professor. Since 2013, he has been the Head of the Research Center of Sensor, Information and Communication Systems, Radio-Frequency Systems Group. He has (co)authored 30 journal publications and more than 40 conference papers. His research interests include measurement and modeling of channels for V2X communication, optimization, and design of optical receivers and transmitters for free-space optics (FSO) systems, influence of atmospheric effects on optical signal propagation, evaluation of FSO availability and reliability, higher order non-uniform sampling and signal reconstruction, and software-defined radio.

MARKUS RUPP received the Dipl.Ing. degree from the University of Saarbrücken, Germany, in 1988, and the Dr.Ing. degree from the Technische Universität Darmstadt, Germany, in 1993. Until 1995, he held a Postdoctoral position with the University of California at Santa Barbara, Santa Barbara, CA, USA. From 1995 to 2001, he was with the Wireless Technology Research Department, Nokia Bell Labs, Holmdel, NJ, USA. Since 2001, he has been a Full Professor of digital signal processing in mobile communications with TU Wien.

ANDREAS F. MOLISCH was with TU Vienna, AT&T (Bell) Labs, Lund University, and Mitsubishi Electric Research Labs. He is currently the Solomon Golomb - Andrew and Erna Viterbi Chair Professor with the University of Southern California. He is the author of four books, 19 book chapters, more than 240 journal papers, 320 conference papers, as well as 80 patents. His research interests include wireless communications, with an emphasis on wireless propagation channels, multi-antenna systems, ultrawideband signaling and localization, novel modulation methods, and caching for wireless content distribution. He is a Fellow of the National Academy of Inventors, the IEEE, AAAS, and IET, as well as a member of the Austrian Academy of Sciences. He was a recipient of numerous awards.

CHRISTOPH F. MECKLENBRÄUKER (S'88–M'97–SM'08) received the Dipl.Ing. degree (Hons.) in electrical engineering from TU Wien, in 1992, and the Dr.Ing. degree (Hons.) from the Ruhr-Universität Bochum, Bochum, Germany, in 1998. From 1997 to 2000, he was with Siemens AG, Austria, where he was engaged in the standardization of the radio access network for UMTS. From 2000 to 2006, he was a Senior Research with the Telecommunications Research Center Vienna (FTW), Vienna. In 2006, he joined the Institute of Communications and Radio Frequency Engineering, TU Wien, as a Full Professor. From 2009 to 2016, he led the Christian Doppler Laboratory for Wireless Technologies for Sustainable Mobility. He has authored approximately 250 papers in international journals and conferences, for which he has also served as a reviewer. He holds several patents in the field of mobile cellular networks. His current research interests include radio interfaces for peer-to-peer networks (vehicular connectivity and sensor networks), ultra-wideband radio, and MIMO transceivers. He is a member of the Antennas and Propagation Society, the Intelligent Transportation Society, the Vehicular Technology Society, the Signal Processing society, VDE, and EURASIP. He is the Councilor of the IEEE Student Branch Wien. His doctoral dissertation received the Gert-Massenberg Prize, in 1998.